



Model of dust thermal emission of comet 67P/Churyumov–Gerasimenko for the Rosetta/MIRO instrument[☆]

Adeline Gicquel^{a,*}, Dominique Bockelée-Morvan^b, Cédric Leyrat^b, Vladimir Zakharov^c, Jacques Crovisier^b, Nicolas Biver^b, Samuel Gulkis^d

^a LERMA, Observatoire de Paris, 5 place Jules Janssen, 92195 Meudon, France

^b LESIA, Observatoire de Paris, CNRS, UPMC, Université Paris-Diderot, 5 place Jules Janssen, 92195 Meudon, France

^c Gordien Strato, 3 allée de la Graineterie, 91370 Verrières le Buisson, France

^d Jet Propulsion Laboratory, California Institute of Technology, 4800 Oak Grove Drive, Pasadena, CA 91109, USA



ARTICLE INFO

Article history:

Received 22 March 2013

Received in revised form

12 June 2013

Accepted 16 June 2013

Available online 22 June 2013

Keywords:

Comets

Rosetta

67P/Churyumov–Gerasimenko

Dust

Millimeter–submillimeter

ABSTRACT

The ESA's *Rosetta* spacecraft will arrive at comet 67P/Churyumov–Gerasimenko in 2014. The study of gas and dust emission is primary objective of several instruments on the *Rosetta* spacecraft, including the Microwave Instrument for the Rosetta Orbiter (MIRO). We developed a model of dust thermal emission to estimate the detectability of dust in the vicinity of the nucleus with MIRO. Our model computes the power received by the MIRO antenna in limb viewing as a function of the geometry of the observations and the physical properties of the grains. We show that detection in the millimeter and submillimeter channels can be achieved near perihelion.

© 2013 Published by Elsevier Ltd.

1. Introduction

Comet 67P/Churyumov–Gerasimenko (67P) was discovered in May 1969 after its perihelion at 1.28 AU. Because of repeated close encounters with Jupiter in 1840 and 1959, the perihelion distance varied from 2.7 AU prior to 1959 to the current value (1.28 AU) and the activity of the comet increased. This increase of the activity likely facilitated its discovery. Comet 67P was observed during the seven perihelion passages since its discovery and an initial characterization of the activity (Osip et al., 1992; Weiler et al., 2004; Lara et al., 2011), of the nucleus properties (Lamy et al., 2007; Tubiana et al., 2008; Kelley et al., 2009) and of the coma environment (Hansen et al., 2007; Agarwal et al., 2007, 2010), has been drawn.

The ESA (European Space Agency) *Rosetta* spacecraft was launched on 2 March 2004, to reach comet 67P in May 2014.

The probe will be inserted into an orbit around the nucleus at a heliocentric distance r_h slightly in excess of 3 AU. The lander *Philae* will be deposited on the nucleus in November 2014 ($r_h \approx 3$ AU). The orbiter will be maintained in the vicinity of the comet until perihelion ($r_h = 1.3$ AU) or even until $r_h \approx 1.8$ AU post-perihelion (December 2015). Thus, nineteen months of uninterrupted, close-up observations of the gas and dust coma will be obtained. The *Rosetta* mission is exceptional because for the first time a spacecraft will place a lander on a comet nucleus and follow the comet during its journey towards the Sun. Scientific instruments on the lander and orbiter will characterize the evolution of comet gas and dust activity during its approach to the Sun.

The goals of the *Rosetta* mission are the global characterization of the nucleus (morphology, surface composition, internal structure) and of the coma (development of the activity, composition and physical properties, dust–gas interaction, interaction with the solar wind) with both *in situ* and remote-sensing instruments. The increase of the nucleus temperature leads to an increase of the production rate accompanied by the development of the coma.

Rosetta carries a wide range of scientific payload (Glassmeier et al., 2007), including the Microwave Instrument for the Rosetta Orbiter (MIRO) (Gulkis et al., 2007) to characterize the nucleus, gas and dust properties of comet 67P.

[☆]This is an open-access article distributed under the terms of the Creative Commons Attribution-NonCommercial-No Derivative Works License, which permits non-commercial use, distribution, and reproduction in any medium, provided the original author and source are credited.

* Corresponding author. Astrochemistry Laboratory, Code 691, NASA GSFC, 8880 Greenbelt Rd., Greenbelt, MD 20771, USA. Tel.: +1 301 6145222.

E-mail address: adeline.gicquel@nasa.gov (A. Gicquel).

In this paper we present a model of dust thermal emission to investigate the detectability of dust with the MIRO instrument as a function of the geometry of the observations and of the physical properties of the grains.

2. MIRO instrument

The MIRO instrument (Gulkis et al., 2007) is a consortium instrument, built and operated at the Jet Propulsion Laboratory, with hardware contributions from the Max-Planck-Institute for Solar System Research, and the Paris Observatory. Basic elements of the instrument are a 30-cm diameter, offset parabolic reflector telescope, and two heterodyne receivers operating at millimeter (190 GHz \approx 1.6 mm) and submillimeter (562 GHz \approx 0.5 mm) wavelengths. The half power beam widths (HPBW) of the MIRO beams are 23.8 ± 1.5 arcmin and 7.5 ± 0.25 arcmin at millimeter and submillimeter wavelengths, respectively. For a typical comet–*Rosetta* spacecraft (S/C) distance $\Delta = 20$ km, the spatial resolutions at the nucleus are 0.138 and 0.044 km at millimeter and submillimeter wavelengths, respectively.

The primary goals of the MIRO instrument are to measure the sub-surface temperatures of the nucleus, the gas production rate, the relative abundances, the velocity and the excitation temperature of gas species, along with their spatial and temporal variability. In particular, MIRO has a very high sensitivity to measure direct outgassing of three volatile species from the nucleus: CO, CH₃OH, NH₃, and three oxygen-related isotopologues of water: H₂¹⁶O, H₂¹⁷O and H₂¹⁸O to obtain the fundamental isotope ratios ¹⁷O/¹⁶O and ¹⁸O/¹⁶O. We refer the reader to Gulkis et al. (2007) for a detailed presentation of the MIRO instrument.

The millimeter receiver is configured with a single, broad-band continuum detector. The submillimeter radiometer is configured with both a broadband continuum detector and a very-high spectral resolution (44 kHz) spectrometer. Both continuum channels operate in total power mode. The 1 to 5-s Allan deviation noise is estimated to be, respectively, 0.11 K and 0.31 K at millimeter and submillimeter wavelengths (Gulkis et al., 2007). These 1– σ receiver noises will allow us to estimate the detectability of dust thermal emission with MIRO. The signal-to-noise ratio of the measurement must be $> 3\sigma$ for a statistically reliable detection.

3. Model of dust thermal emission

Observations at submillimeter and millimeter wavelengths are most sensitive to large particles in the cometary grain size distribution and complement optical and infrared observations, which probe micrometer-sized grains. By measuring the radiation from large particles, we can obtain information on the dust production rate. Jewitt and Luu (1990) showed that a substantial fraction of the total dust mass in comets is contained within the largest grain sizes.

Our model computes the thermal emission of the dust coma measured in the MIRO beam, expressed in antenna temperature scale, which can be compared to the sensitivity of the continuum receivers. We assume that the dust coma contains grains with radii in the range from $a_{\min} = 0.1 \mu\text{m}$ to the maximum liftable size a_{\max} . The antenna temperature T_A is obtained from numerical integration along lines of sight in the field of view

$$T_A = \frac{\lambda^2}{2k_B} \frac{1}{\Omega_A} \iint_{\Omega_{MB}} B_d(\theta, \varphi, \nu) P_N(\theta, \varphi) d\Omega, \quad (1)$$

where k_B is the Boltzmann constant, λ is the wavelength, and ν is the frequency. $P_N(\theta, \varphi)$ is the normalized MIRO beam pattern (i.e., equal to 1 at maximum) approximated by a Gaussian. Ω is the main beam solid angle and Ω_A is the beam solid angle equal to 5.4×10^{-6} and 5.4×10^{-5} sr at $\lambda = 0.5$ and 1.6 mm, respectively. $B_d(\theta, \varphi, \nu)$ is the

spectral brightness (in units of [W m⁻² sr⁻¹ Hz⁻¹]) of the dust grains. We define the spherical coordinate system (z, θ, φ) centered at the *Rosetta* S/C, where z is the radial distance from the S/C along the ray defined by (θ, φ), and $\theta = 0$ corresponds to the center of the beam ($P_N = 1$).

The spectral brightness $B_d(\theta, \varphi, \nu)$ is obtained by numerical integration along z and grain size a :

$$B_d(\theta, \varphi, \nu) = \int_0^\infty \int_{a_{\min}}^{a_{\max}} F_d(a, z, \theta, \varphi, \nu) da dz, \quad (2)$$

where $F_d(a, z, \theta, \varphi, \nu)$ describes the contribution of particles of size a to the emission. In the case of an isotropic coma, $F_d(a, z, \theta, \varphi, \nu)$ is only dependent on the distance r of the point (z, θ, φ) to the center of the nucleus. For thermal emission, the term $F_d(a, z, \theta, \varphi, \nu)$ can be written as

$$F_d(a, z, \theta, \varphi, \nu) = n_d(a, r) \pi a^2 Q_{\text{abs}}(a, \nu) B_\nu(T_d), \quad (3)$$

where $n_d(a, r)$ is the density distribution of grains of size a , T_d is the equilibrium temperature of the grains, and $B_\nu(T_d)$ is the Planck function. T_d can be assumed in first approximation to be independent of the grain size and taken equal to the equilibrium temperature (Jewitt and Luu, 1990). For example we obtained $T_d = 244$ K and 149 K at the heliocentric distances $r_h = 1.3$ AU and 3.5 AU, respectively. The absorption efficiency Q_{abs} is a function of grain size, shape, composition and porosity of the grain.

We used the Mie theory (Bohren and Huffman, 1983; Van de Hulst, 1957), which is the most common technique used throughout the literature (Lisse et al., 1998; Hanner et al., 1996, 1994; Harker et al., 2002), to compute Q_{abs} for spherical grains of given radius and optical constants $m_\nu = n - ik$, where n and k are the wavelength-dependent indices of refraction. Three grain compositions are considered: organics, olivine, and two-layer grains. The two-layer composition is based on the structure of cometary grains outlined by Greenberg and Hage (1990). The basic building block consists of a silicate core surrounded by an organic component. The indices of refraction that we used to calculate Q_{abs} for the amorphous olivine and organics are from Pollack et al. (1994).

The Maxwell Garnett effective medium theory was used to calculate the effective refractive index for the two-layer grains (Greenberg and Hage, 1990). We considered two-layer grains with a fractional mass of the mantle component equal to 50%. We adopt a density of $\rho_{\text{Org}} = 1.5 \text{ g cm}^{-3}$ for organics grains and of $\rho_{\text{Ol}} = 3.5 \text{ g cm}^{-3}$ for olivine grains (Pollack et al., 1994).

In order to simplify the analysis we assume that grains of the same size have the same mass $m_d(a)$ irrespective of their actual composition. We assume that the density of grains is $\tilde{\rho} = 1 \text{ g cm}^{-3}$ which corresponds to a porosity of $\approx 33\%$, 71% and 60% for organics, olivine and two-layer grains, respectively. We used a form of the Maxwell Garnett formula, which is described by Hage and Greenberg (1990), to calculate the refractive indices for porous grains. The indices of refraction at the wavelengths $\lambda = 0.5$ mm and $\lambda = 1.6$ mm used in this study are given in Table 1.

The density distribution of dust grains in the size range ($a, a + da$), which is a term of Eq. (3), is derived from the continuity

Table 1
Optical constants.

Composition	$\lambda = 0.5$ mm		$\lambda = 1.6$ mm		Reference
	n	k	n	k	
Olivine	2.08	4.00×10^{-2}	2.08	3.00×10^{-2}	Pollack et al. (1994)
Organics	2.28	1.90×10^{-2}	2.28	2.80×10^{-3}	Pollack et al. (1994)
Two-layer	2.19	2.82×10^{-2}	2.19	1.46×10^{-2}	This work

Table 2

The nucleus temperature at the sub-solar point and the maximum liftable size for different heliocentric distances and gas production rates.

r_h (AU)	T_{nuc} (K)	Q_g^{max} (kg s ⁻¹)	Q_g^{max} (mol s ⁻¹)	a_{max} (mm)	Q_g^{min} (kg s ⁻¹)	Q_g^{min} (mol s ⁻¹)	a_{max} (mm)
1.3	353	3.81×10^2	1.13×10^{28}	16.5	1.29×10^2	4.14×10^{27}	5.8
2.0	285	9.10×10^1	2.50×10^{27}	3.4	1.58×10^1	4.60×10^{26}	0.6
3.0	232	2.41×10^1	5.40×10^{26}	0.7	2.09	3.70×10^{25}	5.7×10^{-2}
3.5	215	1.73×10^1	3.80×10^{26}	0.5	1.33	2.10×10^{25}	3.3×10^{-2}

equation of the dust flow:

$$n_d(a, r) da = Q_d^i \frac{n(a) da}{4\pi r^2 v_d(a, r)} \quad (4)$$

where $n(a) \propto a^{-q}$ is the size distribution, v_d is the grain velocity along the radial distance from the center of the nucleus r , Q_d^i is the total dust production rate (in units of [s⁻¹]). From the analysis of the dust trail of comet 67P the power index q was estimated to be 3.5 up to 4.1 (Agarwal et al., 2010; Fulle et al., 2010; Ishiguro, 2008; Kelley et al., 2008, 2009). For comet 9P/Tempel 1, Gicquel et al. (2012) inferred $2.8 \leq q \leq 3.1$ from observations with Spitzer undertaken before the Deep Impact experiment. We will investigate size indexes from 2.5 to 4.5.

In the following paragraphs, we will describe the parameters to compute the dust grain velocity. In our model we assume that the distributions of gas density ρ_g and gas velocity v_g along the radial distance from the center of the nucleus r are described by adiabatic spherical expansion of gas from a source of gas where the gas velocity on its surface is equal to the local sound velocity. This expansion is specified by the radius of the source r_n , the gas production rate Q_g , the surface temperature of the nucleus T_n and the gas properties: the molecular mass m_g and specific heat ratio γ (Lamb, 1932; Gombosi, 1994). Adopted values for m_g and γ correspond to mixtures of H₂O, CO₂ and CO gases with relative proportions varying with heliocentric distance (Biele et al., 2012).

We assume that the presence of dust has no impact on the gas and we also neglect collisions between dust grains. The motion of the grain is governed only by the gas drag force F_A and nucleus gravity force F_G . All other forces (i.e., the solar radiation pressure, the solar gravity, etc.) are assumed negligibly small in comparison with F_A and F_G within the domain of simulation. In such conditions, dust grains with mass m_d move radially and variation of the dust grain velocity v_d along the radius is computed by numerical integration of the equations of motion:

$$\frac{dr}{dt} = v_d, \quad m_d \frac{dv_d}{dt} = F_A + F_G \quad (5)$$

with initial condition $v_d=0$ at the nucleus surface.

The nucleus gravitational force F_G is defined as

$$F_G = -G \frac{M_n m_d}{r^2} \quad (6)$$

where $G=6.67 \times 10^{-11}$ m³ kg⁻¹ s⁻² is the gravitational constant and $M_n=1.3 \times 10^{13}$ kg is the mass of the nucleus computed using the estimated 67P nucleus radius of $r_n=2.04 \pm 0.11$ km (Kelley et al., 2009) and a bulk density of 370 kg m⁻³ (Lamy et al., 2007).

The drag force F_A is defined as

$$F_A = \frac{1}{2}(v_g - v_d)^2 \rho_g \pi a^2 C_D \quad (7)$$

where C_D is the drag coefficient of grains. As the gas production rate of comet 67P does not exceed 10^{28} s⁻¹ (Schleicher, 2006), the minimal mean free path of the molecules in the coma is of the order of meters. Since the size of grains is $\ll 1$ m, the gas flow over the grains may be considered as free molecular. Therefore, for the determination of the drag coefficient C_D we use its free molecular expression (Crifo et al., 2005).

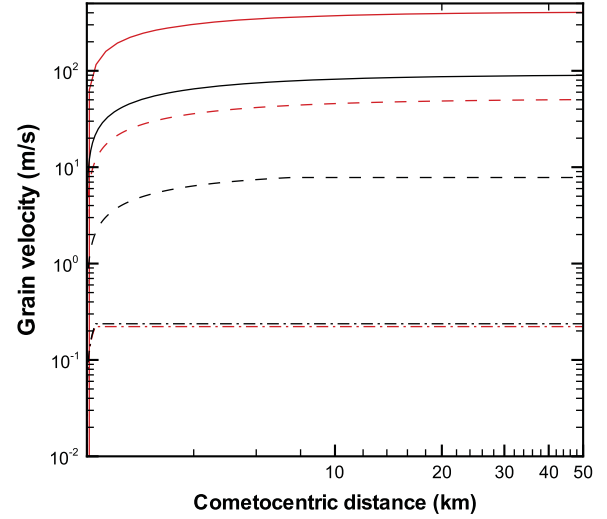


Fig. 1. Grain velocity as a function of distance to nucleus center. The different curves correspond to sizes $a=0.1 \mu\text{m}$ (solid line), $a=10 \mu\text{m}$ (dashed line) and a_{max} (dashed-dotted line). Red and black curves correspond to $r_h=1.3$ AU and $r_h=3.5$ AU, respectively. We used the maximum gas production rates (with the corresponding maximum liftable sizes) given in Table 2. (For interpretation of the references to color in this figure legend, the reader is referred to the web version of this article.)

The maximum ejectable grain size a_{max} is obtained from equality of the drag force and the nucleus attraction at the surface (Crifo and Rodionov, 1997). Therefore, for sonic expansion of the gas and zero initial velocity of the dust grains on the surface and taking into account that $C_D \approx 4$ on the surface

$$a_{max} = \frac{3Q_g \sqrt{\gamma m_g k_B T_n}}{8\pi G \rho M_n} \quad (8)$$

To compute the surface temperature of the nucleus T_n , we supposed that the surface of the nucleus is mainly heated by the Sun. The corresponding surface and sub-surface temperatures will imply sublimation effects and gas production that will drive the velocity of dust. To model the surface temperature of comet 67P, we assume here that heat propagates through the regolith by thermal conduction only. We neglect the sublimation processes for simplicity as we mainly need an estimation of the surface temperature at a given heliocentric distance. The diurnal insolation cycle is computed according to the spin rate derived by Lamy et al. (2007), and heat conduction is computed using a 1-D Crank–Nicolson scheme over 15 thermal skin depths δ_{th} . We refer the reader to Leyrat et al. (2011) for a full description of the thermal model. The nucleus is modeled as a sphere of radius r_n and the temperature is estimated at the equator of the body. We assume a bolometric Bond albedo equal to 0.014 (Groussin et al., 2007) and a thermal inertia $\Gamma = 10$ J m⁻² K⁻¹ s^{-1/2} similar to the value determined for comet 9P/Tempel 1 (Groussin et al., 2007).

We summarize the nucleus temperature at the sub-solar point and the maximum liftable size for different heliocentric distances and gas production rates in Table 2. The maximum (Q_g^{max}) and

Table 3Dust opacities at $\lambda = 0.5$ mm and $\lambda = 1.6$ mm.

Compound	Size index (q')	Size range (mm)	Porosity (%)	$\kappa_{0.5 \text{ mm}}$ ($\text{m}^2 \text{ kg}^{-1}$)	$\kappa_{1.6 \text{ mm}}$ ($\text{m}^2 \text{ kg}^{-1}$)
Olivine	2.0	10^{-4} –16.5	71	8.0×10^{-2}	3.8×10^{-2}
Olivine	2.5	10^{-4} –16.5	71	9.6×10^{-2}	4.0×10^{-2}
Olivine	3.0	10^{-4} –16.5	71	1.2×10^{-1}	4.1×10^{-2}
Olivine	3.5	10^{-4} –16.5	71	1.5×10^{-1}	3.7×10^{-2}
Organics	2.0	10^{-4} –16.5	33	8.6×10^{-2}	1.5×10^{-2}
Organics	2.5	10^{-4} –16.5	33	1.1×10^{-1}	1.6×10^{-2}
Organics	3.0	10^{-4} –16.5	33	1.7×10^{-1}	1.6×10^{-2}
Organics	3.5	10^{-4} –16.5	33	1.9×10^{-1}	1.1×10^{-2}
Two-layer	2.0	10^{-4} –16.5	60	7.6×10^{-2}	2.3×10^{-2}
Two-layer	2.5	10^{-4} –16.5	60	9.2×10^{-2}	2.4×10^{-2}
Two-layer	3.0	10^{-4} –16.5	60	1.2×10^{-1}	2.4×10^{-2}
Two-layer	3.5	10^{-4} –16.5	60	1.3×10^{-1}	1.9×10^{-2}

minimum (Q_g^{\min}) gas production rates correspond to the expected domain of the gaseous activity of comet 67P (Biele et al., 2012).

We show in Fig. 1 the velocity of the grain as a function of the radial distance from the nucleus for various grain sizes and heliocentric distances, using the maximum gas production rates given in Table 2. At a distance of about 10 nuclear radii (≈ 20 km), the dust reaches its terminal velocity.

For comparison with previous studies of dust thermal emission at submillimeter wavelengths from ground based observations (Jewitt and Luu, 1992; Boissier et al., 2012), we have computed the dust opacities (in units of [$\text{m}^2 \text{ kg}^{-1}$]). In first approximation, assuming that the dust velocities scale according to $v_d(a) \propto a^{-0.5}$, the dust opacity κ_λ can be derived as

$$\kappa_\lambda = \frac{\int_{a_{\min}}^{a_{\max}} \pi a^2 Q_{abs}(a, \nu) n'(a) da}{\int_{a_{\min}}^{a_{\max}} (4\pi/3) \bar{\rho} a^3 n'(a) da} \quad (9)$$

with $n'(a) \propto a^{-q'}$ and $q' = q - 0.5$.

Dust opacities at $\lambda = 0.5$ mm and 1.6 mm are given in Table 3 for the maximum size expected at perihelion (case Q_g^{\max}) and a range of size indexes. Values are comparable to those determined by Jewitt and Luu (1992) and Boissier et al. (2012).

4. Results of model simulations

To prepare the planning of the observations, we computed the dust emission in the MIRO beam (expressed in antenna temperature scale T_A) as a function of the heliocentric distance, for different assumptions on the physical properties of the grains and dust coma (composition, size distribution). Calculations were made in limb viewing geometry, since in nadir sounding the measured signal will be dominated by the nucleus thermal emission. We expect T_A to be higher at perihelion because the comet activity is more important. We also expect higher signals for low size indexes q since large grains are more efficient radiators at millimeter and submillimeter wavelengths.

The dust thermal emission expected to be detected with the MIRO instrument was computed assuming a dust production rate Q_d equal to the gas production rate Q_g (in mass) for all heliocentric distances. Fulle et al. (2010) derived a dust mass loss rate of $\sim 400 \text{ kg s}^{-1}$ at perihelion, a value which is close to the expected maximum value of the gas production rate (Table 2). Their dust production rate at 3 AU pre-perihelion is also close to Q_g^{\max} at 3 AU. On the other hand, Fink and Rubin (2012) estimated the dust-to-gas ratio for 67P to 0.03–0.5 at perihelion, with a reasonably likely value of around 0.1. A dust-to-gas ratio of the order of 1 is more consistent with values measured in short-period comets

(e.g. Colangeli et al., 1998). Calculations were performed for heliocentric distances from 1.3 to 3.5 AU. For each distance, we considered the two production rates Q_g^{\min} and Q_g^{\max} corresponding to the expected range of activity of 67P (Table 2).

4.1. Variation with the geometry of observations

In this section, we present the evolution of the signal as a function of heliocentric distance and limb distance. We consider two-layer grains and a size distribution with size index $q = 3.5$. The comet–S/C distance is $\Delta = 20$ km. The signal is computed for a limb viewing geometry, and limb distances δ_{limb} between 0.5 km and 5 km, where δ_{limb} is the distance above the surface. Although, the thermal emission from the dust increases as the boresight distance to the limb decreases, the contribution of the nucleus in the sidelobes also increases. The far side lobes of the antenna are not well characterized at this time, however it is known that a Gaussian beam shape falls off too sharply at large angles from the boresight direction. We estimate that the contribution of the nucleus in the side lobes ranges from 1 K to 0.1 K assuming that the MIRO beam can be represented by a Gaussian sitting on top of a pedestal whose amplitude is -60 dB to -70 dB below the peak gain of the Gaussian. We believe that a conservative estimate is that the power pattern has fallen by -70 dB or more at 0.5 km from the nucleus. At the -70 dB level, the nucleus adds 0.1 K to the antenna temperature which is approximately 10% of the thermal emission from the dust (assumed to be 1 K).

The variation of the signal as a function of heliocentric distance is shown in Fig. 2 for the two MIRO continuum channels and a limb distance $\delta_{limb} = 1$ km. The antenna temperature decreases with increasing heliocentric distance, which can be explained by the decrease of the dust production rate and the dust temperature with increasing heliocentric distance. The antenna temperature at $\lambda = 0.5$ mm is ~ 3 times higher than at 1.6 mm.

The variation of the antenna temperature as a function of limb distance is shown in Fig. 3 for Q_g^{\max} . The antenna temperature decreases with increasing limb distance.

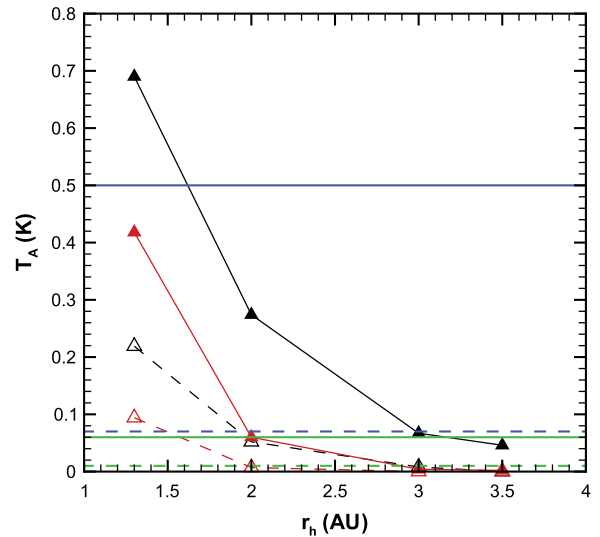


Fig. 2. Antenna temperature for Q_g^{\max} (black) and Q_g^{\min} (red) at $\lambda = 0.5$ mm (solid line) and $\lambda = 1.6$ mm (dashed-line) as a function of the heliocentric distance. We used two-layer grains with a size index $q = 3.5$. The comet–S/C distance is $\Delta = 20$ km and the limb distance is $\delta_{limb} = 1$ km. The horizontal lines show the $3\text{-}\sigma$ detection limits obtained for 1 min on–off cycle (blue) and 1 h on–off cycle (green), at $\lambda = 0.5$ mm (solid line) and $\lambda = 1.6$ mm (dashed-line). The integration time is 5 s on each position. (For interpretation of the references to color in this figure legend, the reader is referred to the web version of this article.)

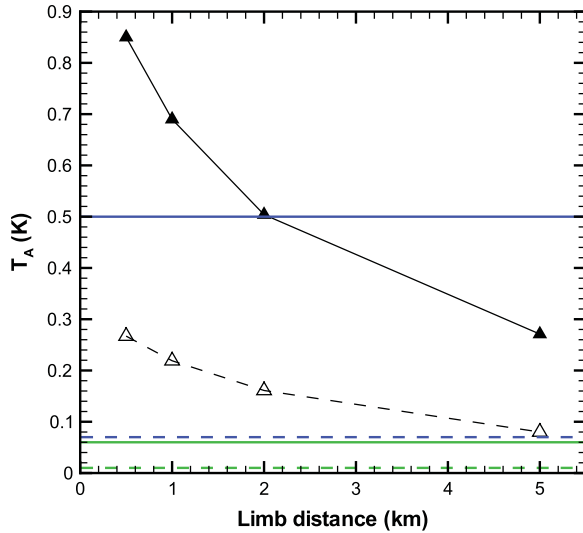


Fig. 3. Antenna temperature for Q_g^{max} at $\lambda = 0.5$ mm (filled) and $\lambda = 1.6$ mm (empty) as a function of the limb distance. We used two-layer grains with a size index $q = 3.5$. The comet–S/C distance is $\Delta = 20$ km. The heliocentric distance is $r_h = 1.3$ AU. The horizontal lines show the $3\text{-}\sigma$ detection limits obtained for 1 min on–off cycle (blue) and 1 h on–off cycle (green), at $\lambda = 0.5$ mm (solid line) and $\lambda = 1.6$ mm (dashed-line). The integration time is 5 s on each position. (For interpretation of the references to color in this figure legend, the reader is referred to the web version of this article.)

4.2. Variation with the physical properties of dust

In this section, we investigate the variation of the dust thermal emission with the physical and compositional properties of the dust.

The variation of the antenna temperature as a function of grain composition is shown in Fig. 4. Results for organics (composition index 1), olivine (composition index 2) and two-layer (composition index 3) grains are displayed for a size index $q = 3.5$. The antenna temperature at $\lambda = 1.6$ mm is strongly sensitive to the grain composition, and the ratio $T_A(\lambda = 0.5 \text{ mm})/T_A(\lambda = 1.6 \text{ mm})$ varies from 2 to 8, with the higher value obtained for the more absorbing grains (organics).

The variation of the antenna temperature as a function of the size index is shown in Fig. 5 for two limb distances (1 and 5 km) and two-layer grains. The relative contribution of small grains increases with the increase of q . The antenna temperature decreases with increasing q because at millimeter and submillimeter wavelengths, the signal is dominated by the emission from large grains.

The ratios $T_A(\lambda = 0.5 \text{ mm})/T_A(\lambda = 1.6 \text{ mm})$ for two-layer grains are, respectively, 2.7, 2.8, 3.1, 3.8 and 5.9 for $q = 2.5, 3.0, 3.5, 4.0$ and 4.5. The signal at 1.6 mm decreases more rapidly with increasing q than the emission at 0.5 mm, as it probes larger sizes. Detection of dust thermal emission in the two MIRO channels would allow to constrain the dust parameters for a more accurate determination of the dust production rate.

5. Detectability with MIRO

The detection of thermal emission from dust using the MIRO instrument is far from an easy task. As indicated in Figs. 2 and 5, the antenna temperatures at 0.5 mm at perihelion and close to the limb for the models considered are < 1 K. The antenna temperatures at 1.6 mm are about three times less. The received power (i.e., the antenna temperature) from the dust is added directly to the receiver noise power, which is estimated to have noise temperatures of ≈ 800 K and ≈ 3600 K at millimeter and submillimeter wavelengths, respectively. To further complicate matters, the dust emission produces a continuum spectrum which will be difficult to separate from the

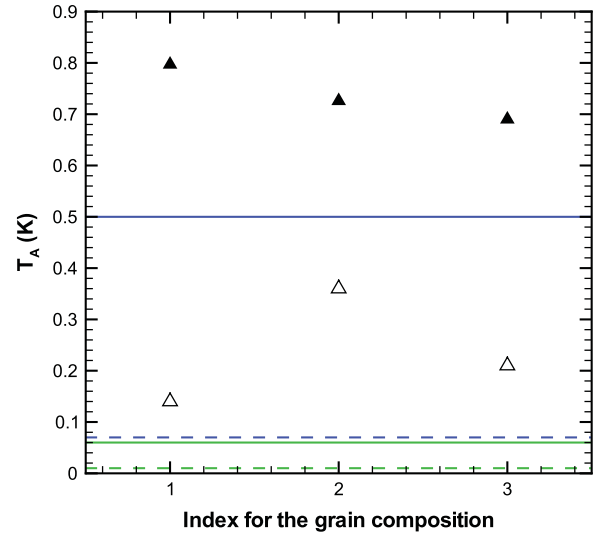


Fig. 4. Antenna temperature for solid organics (index 1), olivine (index 2) and two-layer grains (index 3) at $\lambda = 0.5$ mm (filled) and $\lambda = 1.6$ mm (empty). The size index is $q = 3.5$. The comet–S/C distance is $\Delta = 20$ km. Calculations are for Q_g^{max} at $r_h = 1.3$ AU, and a limb distance $\delta_{limb} = 1$ km. The horizontal lines show the $3\text{-}\sigma$ detection limits obtained for 1 min on–off cycle (blue) and 1 h on–off cycle (green), at $\lambda = 0.5$ mm (solid line) and $\lambda = 1.6$ mm (dashed-line). The integration time is 5 s on each position. (For interpretation of the references to color in this figure legend, the reader is referred to the web version of this article.)

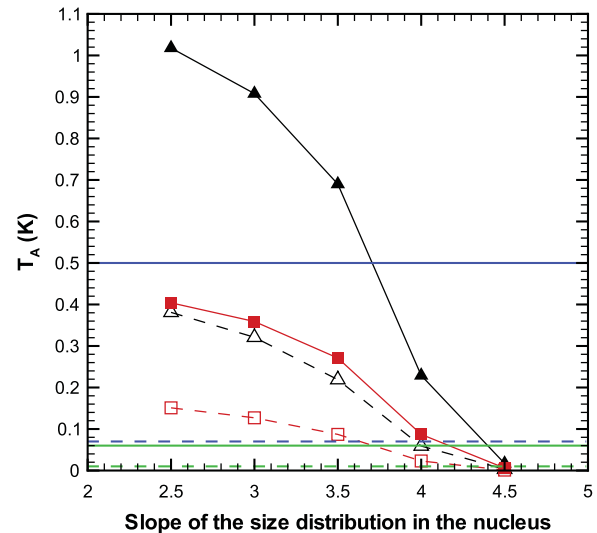


Fig. 5. Antenna temperature as a function of the slope of the distribution at $\lambda = 0.5$ mm (filled) and $\lambda = 1.6$ mm (empty) for two-layer grains. The comet–S/C distance is $\Delta = 20$ km. We used Q_g^{max} at $r_h = 1.3$ AU. The limb distance is $\delta_{limb} = 1$ km (black) and $\delta_{limb} = 5$ km (red). The horizontal lines show the $3\text{-}\sigma$ detection limits obtained for 1 min on–off cycle (blue) and 1 h on–off cycle (green), at $\lambda = 0.5$ mm (solid line) and $\lambda = 1.6$ mm (dashed-line). The integration time is 5 s on each position. (For interpretation of the references to color in this figure legend, the reader is referred to the web version of this article.)

continuum spectrum of the nucleus in the side lobes of the antenna because of the poor signal-to-noise ratio.

Separating the signal from the dust from the radiometer noise requires a position switching strategy. As can be seen in Figs. 2–5, the antenna temperature due to the dust decreases rapidly as the limb distance of the boresight increases away from the limb. For example, in Fig. 3, the antenna temperature at 0.5 mm decreases by ≈ 0.5 K between boresight pointing positions of 0.5 to 5 km. The $1\text{-}\sigma$ receiver noise of the submillimeter receiver is estimated to be ≈ 0.31 K (0.11 K for the millimeter channel) in a 5 s integration time. By position switching between a boresight on the dust and blank

sky, and treating the temperature difference between $T_A(\text{dust})$ and $T_A(\text{sky})$ as an independent measurement, it should be possible to stack many measurements and to greatly improve the signal-to-noise ratio. In a 10 s on–off cycle (5 s on each position), the noise on a differential submillimeter measurement will be 0.4 K (0.02 K in an hour). This yields a signal-to-noise ratio of 15 based on a 3- σ noise level and a 1 K contribution from the dust. Another alternate approach to position switching will be to perform repeated continuous scans away (or towards) from the limb and perpendicular to the limb. This observing mode should be more efficient than position switching, by avoiding start, stop, and settling times associated with position switching. This would allow a greater signal-to-noise ratio for the same integration time mentioned above. For data acquired close to the limb edge, it may be possible to subtract the nucleus thermal emission from the individual scans or stacked scans.

In Figs. 2–5, are plotted the 3- σ detection limits obtained for 1 min and 1 h on–off cycle for comparison with the expected antenna temperatures at 0.5 and 1.6 mm. Detection of dust above the 3- σ threshold is expected at perihelion for both continuum channels, providing the size index $q < 4.0$, which is in the range of expected values for 67P (Fulle et al., 2010). The signal-to-noise ratio is not high enough to provide significant constraints on the size distribution, but might allow us to exclude extreme cases, such as a very steep size distribution or very absorbing material such as pure organic grains.

A dust-to-gas ratio higher than 1 would be more favourable for MIRO detection of dust. In addition, the local gas and dust production rates on certain regions of the nucleus surface (e.g., active areas or subsolar regions) will be probably higher than those considered in our model which assumes isotropic production of dust and gas. However, worth is to note that keeping the dust-to-gas ratio equal to 1, the antenna temperature is not proportional to the dust or gas production rate. We made computations with the parameters of Fig. 2, by assuming that $r_h = 1.3$ AU a gas production rate 10 times higher than Q_g^{max} in Table 2. With respect to results obtained with Q_g^{max} , the antenna temperature increases by a factor of 1.6 and 3.5, at $\lambda = 0.5$ mm and 1.6 mm, respectively. This behaviour can be explained by the 10 times increase of the maximum liftable size (now 17 cm). Most of the dust mass is then in large particles which have a small emitting cross-section.

6. Conclusion

We modeled the thermal emission of dust grains in comet 67P in order to investigate the detectability of the dust coma by the MIRO instrument aboard *Rosetta*. We show that detection in the millimeter and submillimeter channels can be achieved near perihelion. MIRO observations will provide constraints on the dust production of millimeter-sized particles which might complement measurements obtained from the Grain Impact Analyser and Dust Accumulator (GIADA) experiment (Colangeli et al., 2007). MIRO data might also be combined to infrared measurements of dust thermal emission performed with the Visual IR Thermal Imaging Spectrometer (VIRTIS) (Coradini et al., 2007) for further insights into dust properties.

References

Agarwal, J., Müller, M., Grün, E., 2007. Dust environment modelling of comet 67P/Churyumov–Gerasimenko. *Space Science Reviews* 128, 79–131.

Agarwal, J., Müller, M., Reach, W.T., Sykes, M.V., Boehnhardt, H., Grün, E., 2010. The dust trail of Comet 67P/Churyumov–Gerasimenko between 2004 and 2006. *Icarus* 207, 992–1012.

Biele, J., Timm, C., D'Agosta, R., 2012. Rosetta Project Comet Reference Models. ESA Document RO-ESC-TN-5566.

Bohren, C.F., Huffman, D.R., 1983. *Absorption and Scattering of Light by Small Particles*. Wiley, New York.

Boissier, J., Bockelée-Morvan, D., Biver, N., Crovisier, J., Lellouch, E., Moreno, R., Zakharov, V., 2012. Interferometric mapping of the 3.3-mm continuum emission of Comet 17P/Holmes after its 2007 outburst. *Astronomy and Astrophysics* 542, A73.

Colangeli, L., Bussoletti, E., Pestellini, C.C., Fulle, M., Mennella, V., Palumbo, P., Rotundi, A., 1998. ISOCAM imaging of Comets 65P/Gunn and 46P/Wirtanen. *Icarus* 134, 35–46.

Colangeli, L., et al., 2007. The Grain Impact Analyser and Dust Accumulator (GIADA) experiment for the Rosetta mission: design, performances and first results. *Space Science Reviews* 128, 803–821.

Coradini, A., et al., 2007. Virtis: an imaging spectrometer for the Rosetta mission. *Space Science Reviews* 128, 529–559.

Crifo, J.F., Rodionov, A.V., 1997. The dependence of the circumnuclear coma structure on the properties of the nucleus. *Icarus* 127, 319–353.

Crifo, J.-F., Loukianov, G.A., Rodionov, A.V., Zakharov, V.V., 2005. Direct Monte Carlo and multifluid modeling of the circumnuclear dust coma. Spherical grain dynamics revisited. *Icarus* 176, 192–219.

Fink, U., Rubin, M., 2012. The calculation of $Af\rho$ and mass loss rate for comets. *Icarus* 221, 721–734.

Fulle, M., et al., 2010. Comet 67P/Churyumov–Gerasimenko: the GIADA dust environment model of the Rosetta mission target. *Astronomy and Astrophysics* 522, A63.

Gicquel, A., Bockelée-Morvan, D., Zakharov, V.V., Kelley, M.S., Woodward, C.E., Wooden, D.H., 2012. Investigation of dust and water ice in Comet 9P/Tempel 1 from Spitzer observations of the Deep Impact event. *Astronomy and Astrophysics* 542, A119.

Glassmeier, K.-H., Boehnhardt, H., Koschny, D., Kührt, E., Richter, I., 2007. The Rosetta mission: flying towards the origin of the solar system. *Space Science Reviews* 128, 1–21.

Gombosi, T., 1994. *Gaskinetic Theory*. Cambridge University Press, Cambridge, UK.

Greenberg, J.M., Hage, J.L., 1990. From interstellar dust to comets—a unification of observational constraints. *Astrophysical Journal* 361, 260–274.

Groussin, O., A'Hearn, M.F., Li, J.-Y., Thomas, P.C., Sunshine, J.M., Lisse, C.M., Meech, K.J., Farnham, T.L., Feaga, L.M., Delamere, W.A., 2007. Surface temperature of the nucleus of Comet 9P/Tempel 1. *Icarus* 187, 16–25.

Gulkis, S., et al., 2007. MIRO: Microwave Instrument for Rosetta Orbiter. *Space Science Reviews* 128, 561–597.

Hage, J.L., Greenberg, J.M., 1990. A model for the optical properties of porous grains. *Astrophysical Journal* 361, 251–259.

Hanner, M.S., Lynch, D.K., Russell, R.W., 1994. The 8–13 micron spectra of comets and the composition of silicate grains. *Astrophysical Journal* 425, 274–285.

Hanner, M.S., Lynch, D.K., Russell, R.W., Hackwell, J.A., Kellogg, D., Blaney, D., 1996. Mid-infrared spectra of Comets P/Borrelly, P/Faye, and P/Schaumasse. *Icarus* 124, 344–351.

Hansen, K.C., Bagdonat, T., Motschmann, U., Alexander, C., Combi, M.R., Cravens, T.E., Gombosi, T.L., Jia, Y.-D., Robertson, I.P., 2007. The plasma environment of Comet 67P/Churyumov–Gerasimenko throughout the Rosetta main mission. *Space Science Reviews* 128, 133–166.

Harker, D.E., Wooden, D.H., Woodward, C.E., Lisse, C.M., 2002. Grain properties of Comet C/1995 O1 (Hale–Bopp). *Astrophysical Journal* 580, 579–597.

Ishiguro, M., 2008. Cometary dust trail associated with Rosetta mission target: 67P/Churyumov Gerasimenko. *Icarus* 193, 96–104.

Jewitt, D., Luu, J., 1990. The submillimeter radio continuum of Comet P/Borsen–Metcalf. *Astrophysical Journal* 365, 738–747.

Jewitt, D., Luu, J., 1992. Submillimeter continuum emission from comets. *Icarus* 100, 187–196.

Kelley, M.S., Reach, W.T., Lien, D.J., 2008. The dust trail of Comet 67P/Churyumov Gerasimenko. *Icarus* 193, 572–587.

Kelley, M.S., Wooden, D.H., Tubiana, C., Boehnhardt, H., Woodward, C.E., Harker, D.E., 2009. Spitzer observations of Comet 67P/Churyumov–Gerasimenko at 5.5–4.3 AU from the Sun. *The Astronomical Journal* 137, 4633–4642.

Lamb, H., 1932. *Hydrodynamics*. Dover, New York.

Lamy, P.L., Toth, I., Davidsson, B.J.R., Groussin, O., Gutiérrez, P., Jorda, L., Kaasalainen, M., Lowry, S.C., 2007. A portrait of the nucleus of Comet 67P/Churyumov–Gerasimenko. *Space Science Reviews* 128, 23–66.

Lara, L.M., Lin, Z.-Y., Rodrigo, R., Ip, W.-H., 2011. 67P/Churyumov–Gerasimenko activity evolution during its last perihelion before the Rosetta encounter. *Astronomy and Astrophysics* 525, A36.

Leyrat, C., Coradini, A., Erard, S., Capaccioni, F., Capria, M.T., Drossart, P., de Sanctis, M.C., Tosi, F., Virtis Team, 2011. Thermal properties of the asteroid (2867) Steins as observed by VIRTIS/Rosetta. *Astronomy and Astrophysics* 531, A168.

Lisse, C.M., A'Hearn, M.F., Hauser, M.G., Kelsall, T., Lien, D.J., Moseley, S.H., Reach, W.T., Silverberg, R.F., 1998. Infrared observations of comets by COBE. *Astrophysical Journal* 496, 971.

Osip, D.J., Schleicher, D.G., Millis, R.L., 1992. Comets—groundbased observations of spacecraft mission candidates. *Icarus* 98, 115–124.

Pollack, J.B., Hollenbach, D., Beckwith, S., Simonelli, D.P., Roush, T., Fong, W., 1994. Composition and radiative properties of grains in molecular clouds and accretion disks. *Astrophysical Journal* 421, 615–639.

Schleicher, D.G., 2006. Compositional and physical results for Rosetta's new target Comet 67P/Churyumov Gerasimenko from narrowband photometry and imaging. *Icarus* 181, 442–457.

Tubiana, C., Barrera, L., Drahus, M., Boehnhardt, H., 2008. Comet 67P/Churyumov–Gerasimenko at a large heliocentric distance. *Astronomy and Astrophysics* 490, 377–386.

Van de Hulst, H.C., 1957. *Light Scattering by Small Particles*. John Wiley & Sons, Inc., New York.

Weiler, M., Rauer, H., Helbert, J., 2004. Optical observations of Comet 67P/Churyumov–Gerasimenko. *Astronomy and Astrophysics* 414, 749–755.